The Journal of Chemical Physics ARTICLE scitation.org/journal/jcp

Studying vapor-liquid transition using a generalized ensemble

Cite as: J. Chem. Phys. 151, 134108 (2019); doi: 10.1063/1.5116252
Submitted: 23 June 2019 • Accepted: 16 September 2019 •
Published Online: 2 October 2019

Deepti Ballal,[1] Qing Lu,[1] Muralikrishna Raju,[1] and Xueyu Song[2,a)]

AFFILIATIONS

[1]Ames Laboratory, US Department of Energy, Ames, Iowa 50011, USA
[2]Ames Laboratory, US Department of Energy, Ames, Iowa 50011, USA and Department of Chemistry, Iowa State University, Ames, Iowa 50011, USA

[a)]xsong@iastate.edu

ABSTRACT

Homogeneous vapor-liquid nucleation is studied using the generalized Replica Exchange Method (gREM). The generalized ensemble allows the study of unstable states that cannot directly be studied in the canonical ensemble. Along with replica exchange, this allows for efficient sampling of the multiple states in a single simulation. Statistical Temperature Weighted Histogram Analysis Method is used for postprocessing to get a continuous free energy curve from bulk vapor to bulk liquid. gREM allows the study of planar, cylindrical, and spherical interfaces in a single simulation. The excess Gibbs free energy for the formation of a spherical liquid droplet in vapor for a Lennard-Jones system is calculated from the free energy curve and compared against the umbrella sampling results. The nucleation free energy barrier obtained from gREM is then used to calculate the nucleation rate without relying on any classification scheme for separating the vapor and liquid.

I. INTRODUCTION

Nucleation is generally the time limiting step in phase transitions. Understanding the nucleation process is fundamental to our understanding of a wide variety of problems ranging from protein crystallization[1] to atmospheric aerosols[2] and gas foaming in polymers.[3] The free energy barrier separating the local minimum of the metastable phase and the global minimum of the stable phase makes nucleation an activated process.

While there have been attempts to study homogeneous nucleation experimentally,[4–6] getting reliable data has proven to be very difficult.[7] Any tiny impurity can become a nucleation site leading to heterogeneous nucleation, compromising the reliability of the data. In addition, only the nucleation rate can be measured experimentally. Information about the structure and dynamics of the critical nuclei cannot directly be measured since nucleation is a rare event, and when nucleation does occur the system spends very little time at the critical nuclei.[8] Theoretical and computational methods provide an alternative path to studying homogeneous nucleation. One of the earliest theoretical efforts to describe nucleation was the phenomenological approach, Classical Nucleation Theory (CNT).[9,10] According to CNT, two competing factors contribute to the nucleation barrier: the difference in the chemical potential of the two phases which drives the nucleation process and the interfacial free energy cost which opposes nuclei formation. The main assumptions in CNT are that the droplet is an incompressible sphere, the phase inside the droplet has the same properties as the bulk phase, and the interfacial free energy is independent of the size or curvature of the nucleus. Under these assumptions, the free energy of formation of a nucleus, $\Delta G(T, R)$, at temperature T and radius R is given by the competition between the chemical potential difference between the two phases and the free energy required to form an interface,

$$\Delta G(T,R) = \frac{4}{3}\pi R^3 \rho \Delta\mu(T) + 4\pi R^2 \gamma_\infty(T), \tag{1}$$

where ρ is the bulk density of the stable phase, $\Delta\mu(T) = \mu_1(T) - \mu_2(T)$ is the chemical potential difference between the two bulk phases, and γ_∞ is the interfacial free energy (surface tension for the liquid-vapor case) of the planar interface at temperature T. Thus, in CNT, the nucleation barrier can be obtained from the bulk phase properties and the planar surface free energy. This simplicity has led to its popularization and it still remains in use, especially to correlate experimental data.[11]

The maximum of ΔG varying with the droplet size R gives the nucleation barrier ΔG^* for the formation of the critical nucleus. The nucleation rate, J, is given by

$$J = K \exp(-\Delta G^*/k_B T), \tag{2}$$

where K is the kinetic prefactor, k_B is the Boltzmann constant, and T is the temperature. It is essential to have a good estimate for the nucleation barrier, since a small error in ΔG^* leads to an exponential error in the nucleation rate. The many assumptions in CNT lead to an overestimation of the nucleation free energy and an underestimation of the critical nuclei size.[12]

There have been many attempts to get a better quantitative description of nucleation by improving the approximations made in CNT.[13–15] The biggest source of error is due to the use of planar surface tension in Eq. (1). The curvature dependence of surface tension has been extensively studied,[16–20] and it has been established that the surface tension of small droplets is often significantly different from the planar value. Replacing the planar surface tension with the curvature dependent one gives a quantitatively more accurate nucleation free energy,

$$\Delta G(T,R) = \frac{4}{3}\pi R^3 \rho \Delta\mu(T) + 4\pi R^2 \gamma(T,R), \tag{3}$$

where $\gamma(T, R)$ is the surface tension of a sphere of radius R at temperature T. Evaluating the nucleation free energy barrier using the above description still requires the knowledge of the difference in chemical potential of the two phases and the curvature dependent surface tension. These two quantities are most often obtained through different methods requiring multiple simulations. Moreover, $\gamma(T, R)$ is normally calculated from the mechanical route using the normal and tangential pressure profiles, and it is well documented that the thermodynamic and the mechanical routes for calculating the surface tension give different values for the spherical interface.[21,22]

With the advent of computer power, simulations have become more powerful and the nucleation free energy of droplets and the nucleation rate of different sizes can now be accessed without relying on surface tension and chemical potential values. However, the direct simulation of nucleus formation is still not very efficient. Since nucleation is a rare event, the probability of seeing a nucleus form at moderate supercooling is very low and when the nucleus does form, it is difficult to obtain good statistics in the time scale available in simulations.[21,23] Rare event simulation techniques like umbrella sampling,[18,21,24–26] forward flux sampling,[27,28] metadynamics,[29] and transition path sampling[30] are usually employed to study nucleation. ten Wolde and Frenkel[1,21,31,32] were one of the first to apply umbrella sampling[33] to obtain the nucleation barrier. Umbrella sampling still remains the most popular of the biasing techniques to study the structure of droplets during nucleation. However, umbrella sampling is a computationally expensive technique since one needs to simulate several precritical and postcritical nuclei to obtain a single nucleation barrier number.

An alternative to this is the generalized ensemble simulations.[34,35] While umbrella sampling[33] involves applying a mechanical bias so as to change the energy landscape such that a certain region of interest is preferentially sampled, generalized ensemble simulations study the same problem by changing the "sampling weights" in the simulation to effectively sample the region of interest in the energy landscape. Multicanonical Algorithm (MUCA)[36,37] and simulated tempering[38,39] simulation techniques which employ non-Boltzmann sampling are the most well-known of the generalized ensemble methods. The non-Boltzmann sampling helps overcome the broken ergodicity providing efficient sampling. Multicanonical algorithms perform a random walk in the energy landscape, whereas simulated tempering does a random walk in the temperature space. These generalized ensemble methods have been successfully applied to a variety of problems.[36,40–42]

The problem with both multicanonical and simulated tempering methods though is that obtaining the sampling weights requires a time-consuming iterative process. To overcome this problem, Kim *et al.*[43,44] designed an algorithm, the generalized Replica Exchange Method (gREM), which samples along a predefined effective temperature-energy relation. The weights are then obtained from an inverse relationship with the effective temperature. They employ this method with replica exchange to further enhance sampling. The advantage of applying gREM to study the first order phase transition is that multiple critical nuclei (of different shapes and sizes) at different conditions can be observed in the different replicas of the same simulation. This parallelization is a major advantage over umbrella sampling where multiple simulations need to be performed to get the free energy of a single critical nuclei. gREM bears some similarity to the Successive Umbrella Sampling (SUS) method of Virnau and co-workers.[18,19,45,46] In SUS, the entire region to be sampled is subdivided into small density windows and umbrella sampling is applied in the grand canonical ensemble to maintain the system in a certain density range. Probability distribution obtained from this grand canonical simulation can then be used for free energy calculations. Like gREM, SUS can also simulate multiple nuclei in a single simulation. However, in the case of SUS, the number of windows required to span the entire phase transition region is strongly dependent on the size of the system, since the particles' increment from one window to the next is about 10 particles,[46] making simulation of large systems prohibitively expensive. Also, being simulated in the grand canonical ensemble restricts its applicability to Monte Carlo moves. gREM has the advantage here that it can be run using Molecular Dynamics (MD) and has been implemented in the popular LAMMPS package.[47,48]

gREM has been applied to study the vapor-liquid transition and found to predict the coexistence properties very well.[49] Here, we use gREM to study the nucleation free energy of a Lennard-Jones (LJ) liquid nucleus forming in the vapor. The Lennard-Jones potential is an important model potential that has been studied extensively in the literature. gREM can be used to calculate not only the nucleation free energy barrier but also the curvature dependent surface tension. Once $\Delta G(T, R)$ is obtained, the curvature dependent surface tension can be obtained from Eq. (3), since the chemical potential difference between the phases required in Eq. (3) can also be calculated from gREM.

Section II presents a brief overview of the theory of spherical interfaces, the curvature dependent surface tension, and the nucleation rate. This is followed by a discussion on the generalized replica exchange method. In Sec. III, the details of the simulation methodology is described, and Sec. IV presents and discusses the results.

II. THEORETICAL DEVELOPMENT

A. Spherical interface

The theory is written here specifically for a one-component vapor-liquid system. The generalization of the concepts to multicomponent systems is straightforward. For a liquid droplet in the vapor phase, the generalized Laplace equation relates the pressure difference between the interior of the droplet P_l and the vapor pressure P_v, $\Delta p(T, R) = P_l - P_v$, to the surface tension as[50]

$$\Delta p(T,R) = \frac{2\gamma(T,R)}{R} + \frac{\partial \gamma(T,R)}{\partial R}, \tag{4}$$

where R is the size of the droplet and $\gamma(T, R)$ is the surface tension of a droplet of size R at temperature T. The second term on the right-hand side in the above equation is the partial derivative of the curvature dependent surface tension with respect to the radius of the droplet.

At the molecular level, the interface is a few molecular layers thick changing continuously from liquid to vapor. The "size" of the spherical droplet is then somewhat arbitrarily defined. Two of the most frequently used choices are the Gibbs equimolar dividing surface and the surface of tension.[50] The Gibbs equimolar dividing surface (R_e) is defined as the imaginary sharp interface which divides the liquid and vapor region such that there are no excess particles. The number of excess particles, N^x, is defined as

$$N = N_l + N_v + N^x, \tag{5}$$

where N is the total number of particles, $N_l = \rho_l V_l$ and $N_v = \rho_v V_v$. Here, ρ_l is the density inside the liquid sphere and ρ_v is the bulk vapor density. V_l and V_v are the liquid and vapor volumes, respectively. The liquid volume is obtained from the dividing surface, $V_l = 4/3\pi R_e^3$, and the vapor volume is the difference between the total volume and the liquid volume. The Gibbs equimolar dividing surface can also be obtained from the density profile,[16]

$$R_e^3 = \frac{1}{(\rho_l - \rho_v)} \int dr r^3 \frac{d\rho(r)}{dr}, \tag{6}$$

where r is distance from the center of the liquid droplet and $\rho(r)$ is the density profile along the radial direction.

The surface of tension (R_s) is defined as the surface where the surface tension varying with the distance from the center of the droplet goes through a minimum, $\frac{\partial \gamma}{\partial R}\Big|_{R=R_s} = 0$. Setting the derivative of the surface tension in Eq. (3) to zero gives

$$R_s = \left(\frac{3\Delta G}{2\pi\rho_l \Delta\mu}\right)^{1/3}. \tag{7}$$

Equation (4) reduces to the Laplace equation at the surface of tension, $\Delta p(T, R_s) = 2\gamma_s/R_s$.

In the literature, both the Gibbs equimolar dividing surface and the surface of tension have been used to define the "size" of the nuclei. Here, we use R_s since it is the surface of tension that coincides with the critical nuclei and not the Gibbs equimolar dividing surface.[19] The choice of the dividing surface does not change the nucleation free energy barrier, but it does change the numerical value of the curvature dependent surface tension.

B. Curvature dependence of surface tension

The curvature dependence of surface tension has been studied extensively and is a matter of much debate.[16–20] A quantity that is often used in the literature to parameterize the curvature dependence of the surface tension is the Tolman length.[51] The Tolman length, δ, is defined as the difference between the Gibbs equimolar dividing surface and the surface of tension,

$$\delta = R_e - R_s. \tag{8}$$

Tolman related this quantity to the adsorption at the surface of tension, $\Gamma_s = N_s^x/(4\pi R_s^2)$. Here, N_s^x is the excess number of particles at the surface of tension. At constant temperature, the Gibbs-Duhem relation gives[19,50]

$$\left(\frac{\partial \ln \gamma}{\partial \ln R_s}\right)_T = \frac{2\Gamma_s}{R_s(\rho_l - \rho_v)}\left(1 + \frac{2\Gamma_s}{R_s(\rho_l - \rho_v)}\right)^{-1}. \tag{9}$$

Manipulating the expressions for adsorption at the surface of tension and at the Gibbs equimolar dividing surface (which is equal to zero by definition), one can find an expression for the adsorption at the surface of tension as[20]

$$\frac{\Gamma_s}{(\rho_l - \rho_v)} = \delta\left(1 + \frac{\delta}{R_s} + \frac{1}{3}\frac{\delta^2}{R_s^2}\right). \tag{10}$$

Combining the above two expressions gives the Gibbs-Tolman-Koenig-Buff (GTKB) equation,[52]

$$\left(\frac{\partial \ln \gamma}{\partial \ln R_s}\right)_T = \frac{\frac{2\delta}{R_s}\left(1 + \frac{\delta}{R_s} + \frac{1}{3}\left(\frac{\delta}{R_s}\right)^2\right)}{1 + \frac{2\delta}{R_s}\left(1 + \frac{\delta}{R_s} + \frac{1}{3}\left(\frac{\delta}{R_s}\right)^2\right)}. \tag{11}$$

The Tolman length would, in general, be a complex function of the size of the particle. However, Tolman made the assumption that δ is a constant (independent of R_s) and $\delta/R_s \ll 1$.[53,54] Under these conditions, the above equation gives a simple expression for the curvature dependence of surface tension in terms of the planar surface tension, γ_∞, and the Tolman length,

$$\gamma(T, R_s) \approx \gamma_\infty\left(1 - \frac{2\delta}{R_s}\right). \tag{12}$$

Note that in the above expression, the curvature independent δ is in fact the Tolman length in the planar limit, $\delta = \lim_{R_e, R_s \to \infty} = z_e - z_s$.[54]

However, it is known that δ varies strongly with the droplet size.[18,55] Helfrich came up with a phenomenological correction to the above expression[56] using the bending rigidity constant (k) and rigidity constant ($\bar{k}$) as prefactors for the second order correction,

$$\gamma(T, R_s) \approx \gamma_\infty\left(1 - \frac{2\delta}{R_s} + \frac{C}{R_s^2}\right), \tag{13}$$

where the constant $C = (2k + \bar{k})/\gamma_\infty$.

C. Nucleation rate

Once the nucleation barrier $\Delta G^*(T, R)$ is known, the nucleation rate can be calculated. The nucleation rate, according to the classical nucleation picture, can be written as[8]

$$J = Zf_e(N^*)\rho_v e^{-\Delta G^*/k_B T}, \tag{14}$$

where Z is the Zeldovich factor, $f_e(N)$ is the forward rate at which the cluster of size N grows, and N^* is the critical nucleus size. The Zeldovich factor is given by

$$Z = \sqrt{-\frac{\Delta G''(N^*)}{2\pi k_B T}} = \sqrt{\frac{\Delta\mu}{6\pi N^* k_B T}}, \tag{15}$$

where $\Delta G''(N^*)$ is the second derivative of ΔG with respect to N at the critical nucleus size N^*. The second equality is obtained by taking the second derivative of Eq. (3) under the assumption that the R dependent surface tension can be approximated using the critical nuclei surface tension. This should be a reasonable approximation for the postcritical and precritical states near the top of the barrier. The forward rate, f_e, is given by

$$f_e(N) = \frac{A(N)cn_{1,e}\langle|v|\rangle}{4}, \tag{16}$$

where $A(N)$ is the surface area of the liquid droplet and c is the condensation coefficient. $n_{1,e}$ is the monomer density which is approximated using the ideal gas assumption as ρ_v/S, where S is the supersaturation ($S = P/P_{coex}$). $\langle|v|\rangle$ is the average molecular speed approximated to the ideal gas value equal of $\sqrt{8k_BT/\pi m}$, where m is the mass of the molecule.

D. Generalized Replica Exchange Method (gREM)

In this section, gREM, which is used to simulate the different states from pure vapor to pure liquid, is described. gREM along with Weighted Histogram Analysis Method (WHAM)[57–59] postprocessing allows the evaluation of the free energy profile for the first order transformation.

An isobaric-isothermal ensemble simulation cannot effectively sample a first order transition since the energy gap corresponding to the latent heat results in a disjointed probability distribution.[49] A first order transition has a back-bending of the statistical temperature varying with enthalpy. The statistical temperature, T_s, is defined as

$$T_s = \left(\frac{\partial S}{\partial H}\right)^{-1}, \tag{17}$$

where S is the entropy and H is the enthalpy.

At a given temperature, the free energy profile has two minima corresponding to the bulk states and one maximum corresponding to the unstable nuclei state. For the purpose of studying nucleation, it is the unstable state we are interested in. Simulation at a constant temperature would only sample the two bulk states at the free energy minima. gREM[44,60] is an effective technique to study the unstable state. The generalized ensemble changes the sampling to follow a path where the free energy maximum of the unstable state in the canonical ensemble is converted to a minimum in the generalized ensemble. Sampling is done along a parameterized temperature-enthalpy relation for the constant pressure simulation.

Replica exchange further enhances the configurations that are sampled. Replica exchange has been used along with the canonical ensemble to attain better sampling for many systems[61,62] and is easily incorporated in the generalized ensemble as shown by Kim *et al.*[44] In gREM, each replica α has its own "effective" temperature, T_α, and its corresponding sampling weight, W_α.

For a system with M replicas, there are M parallel simulations at different "effective" temperatures. The mapping between the effective temperature (T_α), which varies with enthalpy, and the sampling weight is given by

$$w_\alpha(H) = \int_{H_0}^{H} \frac{1}{T_\alpha(H')} dH', \tag{18}$$

where w_α is the "generalized effective potential" and is related to the generalized ensemble weight W_α by $w_\alpha(H) = -\ln\left(W_\alpha(H)\right)$. H_0 is a reference enthalpy value.

The condition for stability of the nuclei state is given by minimizing the "generalized" free energy, $\beta\mathscr{F}_\alpha(H) = w_\alpha(H) - S(H)$. Minimization of $\mathscr{F}_\alpha$ gives

$$T_s(H^*) = \left(\frac{\partial w_\alpha}{\partial H}\right)^{-1}\Bigg|_{H^*} = T_\alpha(H^*) = T_\alpha^*, \tag{19}$$

where H^* is the enthalpy corresponding to the minimum in the generalized free energy. This means that the probability distribution function is centered around the $T_s(H^*)$ point. The stability condition for this extremum is given by the second derivative of the generalized free energy being negative,

$$\beta\mathscr{F}_\alpha''(H^*) = \frac{T_s'(H^*) - T_\alpha'(H^*)}{T_\alpha^*} < 0. \tag{20}$$

The simplest parameterization for the effective temperature as a function of enthalpy is a straight line,

$$T_\alpha(H) = \lambda_\alpha + \gamma(H - H_0). \tag{21}$$

The parameters λ_α and γ are the intercept and slope of the straight line along which the search for the generalized free energy minimum is performed. The slope γ is chosen to be sufficiently negative to make sure that Eq. (20) is satisfied for all values of H, and $T_\alpha(H)$ intersects with the statistical temperature curve only once. This linear parameterization of effective temperature gives weights that have a generic form of the Tsallis weights.[44]

Exchange of configurations between two replicas α and α' is attempted periodically and accepted with the weight,

$$A_{\alpha,\alpha'} = min[1, \exp(\Delta)], \tag{22}$$

where $\Delta = w_\alpha(H) + w_{\alpha'}(H') - w_\alpha(H') - w_{\alpha'}(H)$. Here, H is the enthalpy of the configuration in the α replica and H' is the enthalpy of the configuration in the α' replica. Exchange between adjacent replicas occurs when there is an overlap in the energy distribution; as system size increases, the distributions become narrower and exchange reduces. As the system size increases, more replicas are required for efficient sampling.[43,63]

Once the probability distribution function is obtained in the generalized ensemble with multiple replicas, the Weighted Histogram Analysis Method (WHAM)[57–59] is used to stitch together

the distribution functions from the different replicas. WHAM converts the biased distribution function into the unbiased continuous free energy curve from the bulk vapor to bulk liquid. Since WHAM calculations can get very intensive because of iterative evaluations of the partition function, we use the recently developed iteration-free approximation called the Statistical Temperature WHAM (ST-WHAM).[64] ST-WHAM speeds up the process of stitching up independent probability distributions to give a single free energy profile at no loss of accuracy, the effectiveness of which has been tested for multiple systems.[64–66]

The density of states (DOS) is given by

$$\Omega(H) = \frac{\mathscr{H}(H)}{\sum_\alpha N_\alpha W_\alpha(H)/\Delta_\alpha}, \tag{23}$$

where $\mathscr{H}(H) = \sum_\alpha \mathscr{H}_\alpha = N_\alpha P_\alpha$, where N_α and P_α are number of samples and probability distribution functions in replica α, respectively. W_α is the generalized ensemble weight and Δ_α is the relative partition function. The partition function depends on DOS, $\Delta_\alpha = \sum_H \Omega(H) W_\alpha(H)$. In the WHAM formulation, these two equations are solved iteratively to obtain the partition function. Once the partition function is known, all other properties can be obtained from statistical mechanical relations.

In ST-WHAM, instead of working with the extensive quantities, one works with the derivative quantities. The inverse temperature is the derivative of the log of DOS,

$$\frac{1}{k_B T_s} = \frac{\partial \ln \Omega}{\partial H} = \sum_\alpha \frac{\mathscr{H}_\alpha}{\mathscr{H}}\left[\frac{\partial}{\partial H}\ln\left(\frac{\mathscr{H}_\alpha}{N_\alpha W_\alpha/\Delta_\alpha}\right) + \frac{\partial}{\partial H}\ln\left(\frac{N_\alpha W_\alpha/\Delta_\alpha}{\sum_{\alpha'} N_{\alpha'} W_{\alpha'}/\Delta_{\alpha'}}\right)\right]. \tag{24}$$

In ST-WHAM, the second term is neglected, which makes iterations to get the partition function unnecessary. Kim *et al.*[64] have shown that neglecting the second term does not affect the accuracy of the results. We compared the ST-WHAM to WHAM for our simulation data, and both methods lead to the same result.

Once the statistical temperature is known, the entropy and Gibbs free energy as a function of the enthalpy are obtained using

$$S(H) = \int \frac{dH}{T_s(H)}, \qquad G(H) = H - T_s(H)S(H). \tag{25}$$

III. SIMULATION METHODOLOGY

In this work, the cut-and-shifted Lennard-Jones potential is used,

$$\beta u(r) = \begin{cases} \beta u_{LJ}(r) - \beta u_{LJ}(r_c) & \text{if } r < r_c, \\ 0 & \text{if } r \geq r_c, \end{cases} \tag{26}$$

where r is the distance between particles and $\beta = 1/k_B T$. The Lennard-Jones potential is $u_{LJ}(r) = 4\varepsilon\left[(\sigma/r)^{12} - (\sigma/r)^6\right]$. Here, r_c is the cutoff distance, σ is the diameter of the particles, and ε is the interaction energy. No long range corrections are added. $r_c = 2.5\sigma$ is used for all the calculations except the nucleation rate calculations where $r_c = 5.0\sigma$ is used to allow comparison with the literature values using the higher cutoff.

The system consists of 2744 particles in a cubic box for all simulations, except those analyzing the planar interface. A system size convergence test was performed to ensure that the free energy numbers obtained from the simulation were independent of the number of particles. gREM implemented in LAMMPS[47] is used to run the simulations.[48] The Nose-Hoover barostat and thermostat are used. A time step of 0.005τ is used, where $\tau = t\sqrt{\varepsilon/m\sigma^2}$. All the quantities presented here are in reduced LJ units: temperature is given in the units of $k_B T/\varepsilon$, pressure in the units of $P\sigma^3/\varepsilon$, density in the units of $\rho\sigma^3$, and distance is z/σ.

To set up the parameters for gREM, two short NPT simulations were run at the extremes of the range of interest. The enthalpy $\tilde{H}_1$ and $\tilde{H}_2$ are obtained at the two temperatures T_1 and T_2. The reference enthalpy in Eq. (21), H_0, is set equal to $\tilde{H}_1$, and the intercept λ_1 of the first replica is set to T_1 and λ_M of the last replica is set to $T_2 - \gamma(\tilde{H}_2 - \tilde{H}_1)$. All the other intercepts, $\lambda_2 \ldots \lambda_{M-1}$, are placed in between these two limits. An initial run with equally spaced replicas is performed. If any discontinuity in the probability distribution function is found, a few more replicas are manually added to ensure complete sampling. The slope γ is selected such that it is more negative than the largest slope of the T_s curve. This is usually found by trial and error. The initial condition for all replicas is a simple cubic lattice at a liquidlike density. For all the thermodynamic calculations, exchange was set at 100 000 steps, except for the simulations where the pressure and density profile were calculated. In that case, there was no exchange, and a single walker was followed to get the statistics. The simulations were run for $1.6 * 10^7$ steps after equilibration for $4 * 10^6$ steps. The postprocessing analysis was done using scripts written in python.[67]

For all the simulations, the pressure of the whole system was set to a predefined pressure. However, for the planar case, setting overall pressure gives a bulk pressure that is higher than the set pressure because of the dip in the tangential pressure of the planar interface (discussed in more detail in Sec. IV B). So, for the case of the planar interface, a set of NP_{zz} gREM simulations were performed where only the normal pressure is set to a predefined pressure and the pressure in the tangential directions is allowed to respond to the normal pressure.

To obtain the pressure profile, we used a modified version of the patch to LAMMPS by Nakamura *et al.*[68] The pressure patch implements the Irving-Kirkwood contour integration[69] and was used to get the tangential and normal pressure profiles. The pressure and density profile was obtained by following a replica and averaging over $1.2 * 10^7$ steps after allowing for equilibration over $4 * 10^6$ steps. The temperature of the replica is taken to be the arithmetic mean of all the temperatures visited by the replica during the production cycle. While the replica visits several temperatures around the mean and the sampling is non-Boltzmann, we still find the averaging for density and pressure from a replica matches that from a canonical ensemble.

The error analysis was done using the bootstrapping method.[70] Fifty different datasets are "generated" by randomly picking samples from the original dataset obtained from gREM allowing for duplication. These datasets are now treated as independent samples and are then used to calculate the average and variance.

IV. RESULTS AND DISCUSSION

This section describes the results from the gREM simulation. The prediction of the coexistence properties is discussed in Subsection IV A. This is followed by a study of the interfacial properties at the planar and spherical interface. Finally, the nucleation rates from gREM are compared with those from direct simulation.

A. Coexistence

While the effectiveness of using gREM for studying the vapor-liquid coexistence of Lennard-Jones fluid has previously been shown,[49] we discuss it here briefly for completeness. Figure 1 shows the temperature varying with enthalpy for pressure $P = 0.028$ through a first order vapor-liquid transition. In the thermodynamic limit, $N \to \infty$, the T-H curve would be a horizontal line through the transition and the two phases would coexist according to the level rule. The states that would be metastable or unstable in the thermodynamic limit are rendered stable in the finite system. In the limit of infinite number of particles, the system would nucleate instantaneously and not stay in the metastable or unstable states.[46]

In Fig. 1, the low enthalpy region on the left is the stable liquid. As the enthalpy is increased, the temperature of the stable liquid increases. Once the coexistence point is crossed, the one phase liquid is now metastable (the vapor is the stable state at this temperature). The temperature rises until the bubble evaporation-condensation transition point is reached.[71] At this point, the first vapor bubble appears and the temperature starts to decrease. As the enthalpy increases, the spherical bubble becomes bigger in size and finally transitions to cylindrical bubbles (configuration not shown in the figure). With a further increase in enthalpy, the cylinder transitions to a planar interface between the liquid and vapor. The planar interface should occur at the coexistence temperature, but in gREM, the planar interface occurs at a temperature slightly above the coexistence temperature. This discrepancy is explained in the planar interface section (Sec. IV B). As the enthalpy is further increased, the vapor becomes the dominant phase and the nuclei is a liquid cylinder. This is followed by the appearance of spherical liquid droplets. Finally, the liquid phase disappears and the system is present as a metastable vapor phase. Further increase in enthalpy results in a rise of temperature, and after the coexistence temperature is crossed, the vapor phase is stable. Figure 2 shows the Gibbs free energy varying with the temperature obtained using Eq. (25) for $P = 0.028$. The coexistence point can be obtained from the intersection of the liquid and vapor branches of the G-T curve or from an equal area construction (similar to the Maxwell construction) of the inverse temperature curve.[49] Figure 3 shows the pressure vs temperature coexistence plot compared against the data from MD simulations.[16] In Fig. 3, the expression that Vrabec *et al.* fit to their MD data is shown: $\ln(p) = 3.166\,4 - 5.980\,8/T + 0.014\,98/T^3$.

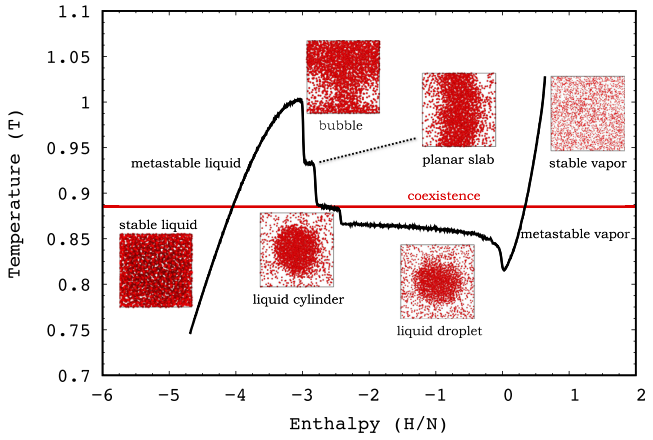

FIG. 1. Temperature vs enthalpy for the vapor-liquid transition at a pressure of 0.028. Shown along the curve are different configurations formed from left to right—stable liquid, metastable liquid, spherical bubble, planar interface, liquid cylinder, liquid spherical droplet, metastable vapor and stable vapor. The configurations shown here are not to scale. The red horizontal line is the coexistence temperature.

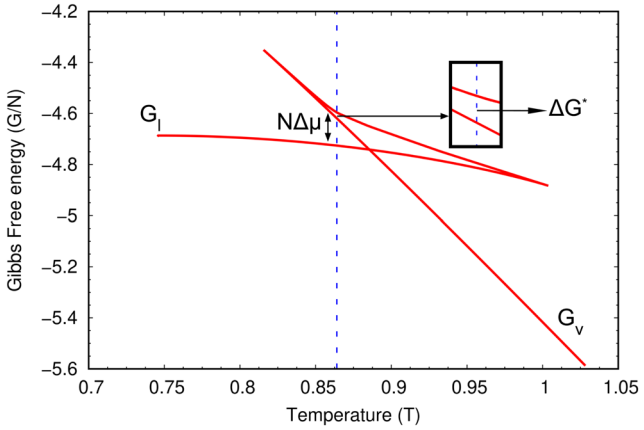

FIG. 2. Gibbs free energy vs temperature at a pressure of 0.028. Also shown are the Gibbs free energy difference, ΔG^*, between the spherical liquid droplet and the metastable vapor phase (in the inset), and the chemical potential difference times the number of particles, $N\Delta\mu$, between the metastable vapor state and the stable liquid state at temperature, $T = 0.864$.

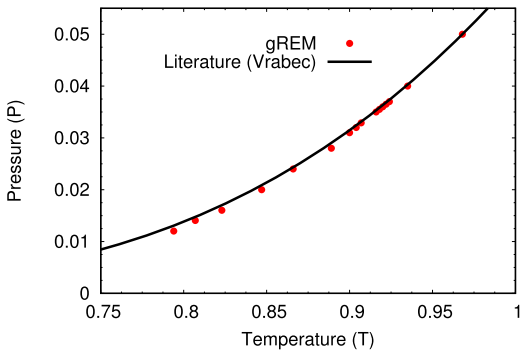

FIG. 3. Temperature vs pressure coexistence curve. Red dots are the values obtained from gREM, and the black curve are the data using the expression from Vrabec *et al.*[16]

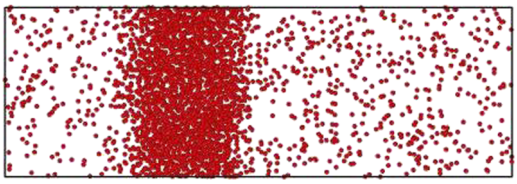

FIG. 4. Planar interface configuration using the NP gREM scheme (where the total pressure is set) at $P = 0.028$. The z-dimension is 3 times the length in x and y dimensions.

B. Planar interface

Planar interface results shown here are with an elongated box with the z-dimension being 3 times the x and y and contains 3000 particles. An elongated box is used to obtain a thicker liquid slab. The bulk liquid is in the center and bulk vapor is on both sides in the configuration shown in Fig. 4.

Figure 5 shows the normal and tangential pressure profile varying with the distance perpendicular to the interface for the planar interface. The simulation is performed with the pressure of the entire system set to $P_{set} = 0.028$. Normal pressure remains constant across the interface, as required by the mechanical equilibrium condition, while the tangential pressure dips at the interface. As shown in Fig. 5, the bulk vapor pressure is higher than the set pressure of 0.028. This is because the total pressure of the system is maintained and in the case of an interface, where there is a dip in the tangential pressure, the bulk pressure has to be larger than P_{set} to get a total pressure equal to P_{set}. The planar interface occurs at temperature $T = 0.908$ which is higher than the coexistence temperature $T = 0.885$ for this pressure. It is, however, the coexistence temperature for a pressure of $P = 0.033$, which is roughly the vapor pressure in Fig. 5. The planar interface for a cubical box occurs at temperature $T = 0.93$ (as in Fig. 1), so elongating the box brings the temperature at which the planar interface occurs closer to the coexistence temperature. This is because for the elongated box, the ratio of the interfacial region to the bulk region is reduced and the effect of interfacial dip on the total pressure is lower. In the limit of infinite size in the z-dimension, the planar interface should occur at the coexistence temperature.

For the planar case, since the normal pressure remains constant throughout the interface, a possibility is to set the normal pressure to the required bulk vapor pressure. This scheme, NP_{zz} gREM, where only the normal pressure is restricted to a certain value (tangential pressure is not explicitly controlled, but responds to the normal pressure) gives the density and pressure profile shown in Fig. 6. The bulk vapor pressure does indeed go to the set pressure now and the planar interface now occurs in gREM at the coexistence temperature $T = 0.885$. The surface tension for the planar interface can be calculated from the pressure profile using the mechanical route as[50]

$$\gamma_{p,m} = \int dz(P_N(z) - P_T(z)). \tag{27}$$

For $T = 0.885$, the surface tension obtained is $\gamma_{p,m} = 0.25$ which compares well with the value obtained from Vrabec's relation,[16]

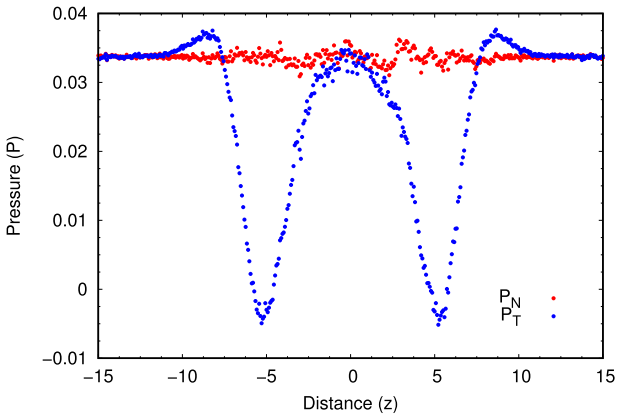

FIG. 5. Planar interface pressure profile using the NP gREM scheme where total pressure is set at $P = 0.028$. Red dots are the normal pressure, P_N, and blue dots are the tangential pressure, P_T. Here, the slab configuration occurs at temperature $T = 0.908$.

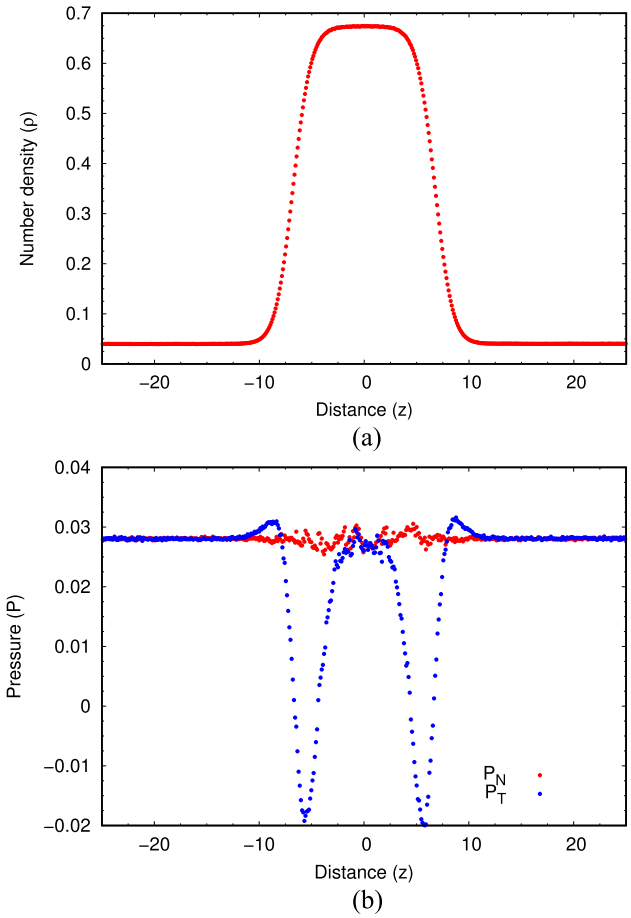

FIG. 6. Planar interface profiles using the NP_{zz} gREM scheme where normal pressure is set at $P = 0.028$. (a) Density profile and (b) pressure profile showing normal pressure (P_N) with red dots and tangential pressure (P_T) with blue dots. Here, the slab configuration occurs at the coexistence temperature $T = 0.885$ and $P = 0.028$.

$\gamma = 2.08(1 - T/T_c)^{1.21} = 0.26$. Here, T_c is the critical temperature equal to 1.0779.

Surface tension can also be calculated from the Gibbs free energy (thermodynamic route) as

$$\gamma_{p,t} = \frac{G - N\mu}{A}, \tag{28}$$

where G is the Gibbs free energy of the system with the planar interface, μ is the chemical potential which is equal for the liquid and the vapor, $\mu = G_l/N = G_v/N$, and A is the cross-sectional area. G_l and G_v are the liquid and vapor free energy at the coexistence temperature, respectively. Since the planar interface that gREM samples in the isobaric ensemble is not at the right pressure, we cannot get a value for the planar interface surface tension from the thermodynamic route. It should be noted that this should not be a problem for the solid-liquid interface since the density difference between the solid and liquid is not as large as the vapor-liquid system. It has been verified that the planar interface does occur at the coexistence temperature for the solid-liquid system.[72]

While the NP_{zz} gREM method gives the planar interface with the right vapor pressure, it cannot be integrated with the other configurations (spheres and cylinders) obtained from NP gREM to get the free energy since these two are fundamentally different simulations. The NP_{zz} gREM method can only be applied to the planar interface since only in the planar interface the normal pressure is constant. For the spherical and cylindrical interfaces, the mechanical equilibrium condition gives a different relation between the normal and tangential pressures.

We also note that this problem does not occur for the spherical interface. In the spherical case, the bulk vapor pressure does indeed go to the set pressure [as shown in Fig. 7(b)]. We have compared the density and pressure profiles for the spherical interface from gREM with profiles from an NVT simulation at the same condition and found that the two profiles match well. We also emphasize that the error in sampling the planar state does not affect the free energy of formation of a spherical liquid droplet since the integration path from the vapor state to the droplet state does not go through the planar interface.

Finally, the problem here is due to the constant pressure constraint on the system and not the generalized ensemble algorithm. Running the gREM in the grand canonical ensemble with T_α varying with $U - \mu N$ instead of H should lead to the planar interface being sampled correctly as has been shown by other methods in the $\mu V T$ ensemble.[46]

C. Spherical interface

Figure 7(a) shows the density profile for a spherical droplet at pressure $P = 0.028$ and average temperature $T_{avg} = 0.864$ in a cubic box. The averaging for the profile is done by following a single walker. Also shown in the figure are the Gibbs dividing surface (R_e) and the surface of tension (R_s) obtained using Eqs. (6) and (7), respectively. The qualitative trends in surface tension or the Tolman length do not change based on the choice of the dividing surface, and only a small quantitative difference can be seen. Finally, we have fit the density profile to a hyperbolic tangent function that is used to obtain the bulk liquid and vapor density [see Eqs. (18) and (19) of Ref. 16].

Figure 7(b) shows the normal (P_N) and tangential (P_T) pressure profiles for the spherical interface. We have verified that the normal and tangential profiles satisfy the mechanical equilibrium condition, $\nabla \cdot \boldsymbol{P} = 0$, which in spherical coordinates is given by[50]

$$P_T(r) = P_N(r) + \frac{r}{2}\frac{dP_N(r)}{dr}, \tag{29}$$

where the second term is the derivative of the normal pressure with respect to the distance from the center of the sphere. The above condition confirms that the droplet is in mechanical equilibrium.

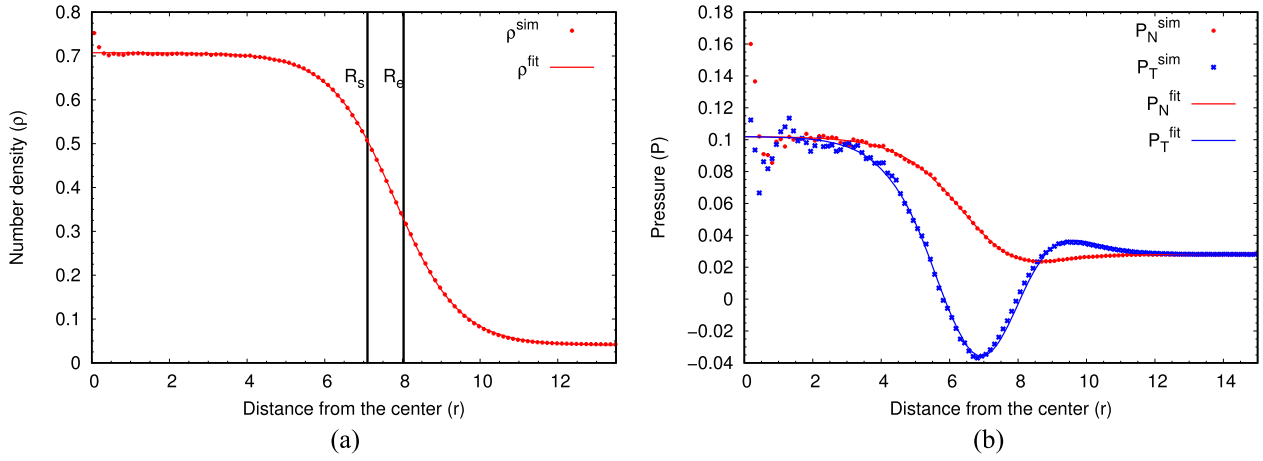

FIG. 7. Spherical interface at pressure p = 0.028 and T = 0.864. (a) Density profile varying with the distance from the center of the sphere. Spheres are the simulated data (ρ^{sim}) and the line is the fit (ρ^{fit}). The Gibbs equimolar dividing surface $R_e = 8.03$ and the surface of tension $R_s = 7.1$ are also shown. (b) Normal and tangential components of the pressure tensor varying with the distance from the center of the spherical droplet. The red spheres and blue squares are normal (P_N^{sim}) and tangential (P_T^{sim}) pressures obtained in the simulation, respectively. The red line is the fit to the normal pressure (P_N^{fit}) and the blue line is the tangential pressure (P_T^{fit}) obtained from the mechanical equilibrium condition [Eq. (29)], thus verifying the mechanical equilibrium condition.

Next, the chemical potential inside and outside the droplet is compared to check for chemical equilibrium, i.e., $\mu_l(T, P_l) = \mu_v(T, P_v)$. Here, μ_l and μ_v are the liquid and vapor chemical potentials at temperature T and liquid (P_l) and vapor (P_v) pressures, respectively. P_l and P_v are obtained from hyperbolic tangent fits to the normal pressure profile similar to what was done for the density profile [see Eq. (22) from Ref. 16]. From the G-T curve (Fig. 2), $\mu_v(T, P_v) = G_v(T, P_v)/N$ and $\mu_l(T, P_v) = G_l(T, P_v)/N$, where N is the number of particles in the system. The chemical potential at the liquid pressure is obtained by thermodynamic integration, $\mu_l(T, P_l) = \mu_l(T, P_v) + \int_{P_v}^{P_l} dp/\rho_l$. A series of NPT simulations were performed from P_v to P_l at the temperature T to get the density ρ_l as a function of pressure. Using this method, we verified that the chemical potential inside and outside the droplet is indeed the same. For the sphere shown in Fig. 7(a), the vapor pressure is $P_v = 0.028$, the liquid pressure inside the sphere (from the fit) is $P_l = 0.102$, and the temperature is $T = 0.864$. From the G-T curve in Fig. 2, $\mu_v(T, P_v) = -4.619$ and $\mu_l(T, P_v) = -4.726$. From NPT simulations, the integral value $\int_{P_v}^{P_l} dP/\rho_l = 0.105$ which gives $\mu_l(T, P_l) = -4.621$. The error in $\mu_v(T, P_v)$ and $\mu_l(T, P_l)$ is of the order of 10^{-5}. The error in the chemical potential equality is about 0.04%.

Now that it has been established that the spherical droplet is in chemical and mechanical equilibrium, we can obtain the nucleation free energy of the spherical droplet from the G-T curve (Fig. 2). Figure 8 shows a comparison of nucleation free energies with the literature values for different supersaturations with the numerical values given in Table I. We note here that gREM is most useful for nuclei with larger cluster size, while it is easier to do umbrella sampling for smaller cluster size. For all conditions, gREM is in reasonable agreement with the literature values. An advantage of gREM is that no classification scheme is required to artificially separate the particles to be "vapor" and "liquid" to obtain the nucleation free energy barrier. Mechanical bias algorithms like umbrella sampling require a classification to apply the bias and it has been shown in the case of liquid-solid transition that the nucleation free energy profile is classification dependent.[73]

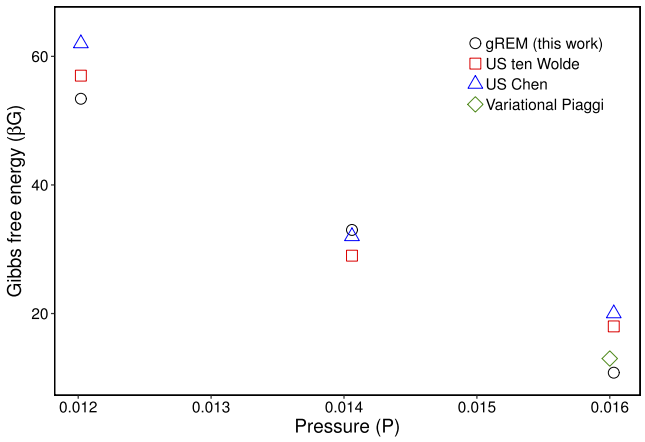

FIG. 8. Nucleation free energy barrier comparison with the literature values for various pressures at temperature $T = 0.741$. Black circles are the gREM results from this work, red squares are the umbrella sampling results from ten Wolde and Frenkel (US ten Wolde),[21] blue triangles are the umbrella sampling results from aggregation-volume-bias Monte Carlo simulations of Chen *et al.* (US Chen),[26] and the green diamonds are from the variational approach of Piaggi *et al.* (Variational Piaggi).[74]

TABLE I. Nucleation free energy barrier comparison with the literature values for various pressures at temperature $T = 0.741$. gREM results from this work are compared against the literature values.

P	$\beta\Delta G^*_{gREM}$	$\beta\Delta G^*_{lit}$
0.01202	53.4 ± 0.2	57[a], 62[b]
0.01406	33.0 ± 0.2	29[a], 32[b]
0.01603	10.8 ± 0.1	18[a], 20[b], 13[c]

[a]Umbrella sampling results from Ref. 21.
[b]Umbrella sampling results from aggregation-volume-bias Monte Carlo simulations of Chen *et al.*[26]
[c]Variational approach of Piaggi *et al.*[74]

D. Tolman Length

Since gREM gives both ΔG^* and the chemical potential difference between the liquid and vapor, $\Delta\mu(T, P_v) = \mu_l(T, P_v) - \mu_v(T, P_v)$, the curvature dependent surface tension for the critical nuclei is obtained from Eq. (3) as

$$4\pi R^2\gamma(R^*, T) = \Delta G^*(T, P_v) - \frac{4}{3}\pi R^{*3}\rho_l\Delta\mu(T, P_v). \quad (30)$$

Here, ρ_l is the liquid density inside the nucleus obtained from the fit to the density profile and R^* is the radius of the critical nucleus. For the curved interface, there are two degrees of freedom[75] such that the quantities T, P_v, and R^* are intrinsically related. Once two of these three quantities are defined, the third is automatically fixed. We use the surface of tension (R_s) to define the radius of the droplet R^*.

Figure 9 shows the ratio of the curvature dependent surface tension to its planar value varying with the curvature ($1/R_s$) for

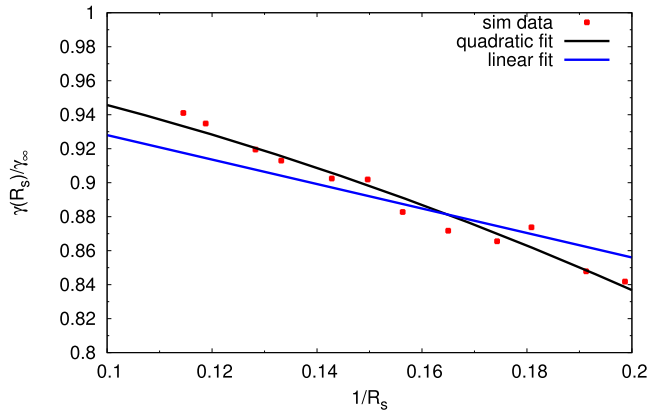

FIG. 9. Ratio of curvature dependent surface tension to the planar value varying with the inverse size of the droplet for temperature $T = 0.9$. Red dots are simulation data, the black line is a second order polynomial fit $[\gamma(R_s)/\gamma_\infty = 1 - 0.27/R_s - 2.73/R_s^2]$, and the blue line a linear fit $[\gamma(R_s)/\gamma_\infty = 1–0.72/R_s]$.

temperature $T = 0.9$. Twelve simulations were performed at pressures of 0.0351 and 0.035 25–0.037 75 at 0.0025 intervals, and spherical droplets formed at these different pressures at a single temperature ($T = 0.9$) were studied. Since the simulations are performed in a constant pressure ensemble, large variation in the droplet size can be accessed. Smaller droplets (larger $1/R$) at $T = 0.9$ were sampled at pressures greater than 0.037 75, but we fit to just the larger droplets because the assumptions in the expression being fit are better for larger droplets. It has also been shown that fitting to the larger droplets gives most reliable results.[54]

We fit both a linear equation [Eq. (12)] and a second order equation [Eq. (13)] to the simulation data to obtain the Tolman length. For the planar surface tension, we use the expression $\gamma_\infty(T) = 2.08(1 - T/T_c)^{1.21}$ from Vrabec *et al.*[16] As shown in Fig. 9, the second order equation is a much better fit. The magnitude and sign of the Tolman length is a matter of great controversy with negative values generally obtained in DFT calculations while MD simulations giving both negative and positive values.[18,19,54,76–79] The fit in Fig. 9 to the second order equation gives a Tolman length $\delta(T = 0.9) = +0.14$. DFT calculations by Blokhuis and van Giessen[76] report a value of around −0.1, van Geissen and Blokhuis[54] report two different numbers: a value of −0.1 using Δp obtained from simulations of the spherical interface and a value of +0.2 from the planar interface simulations. They also reported a value of +0.264 obtained from MD simulations of spheres in a previous publication.[78] Haye and Bruin[80] reported a value of +0.2 from MD simulations of droplets. The reason for the discrepancy in the above numbers is not clear, but as pointed out by van Geissen and Blokhuis[54] even a small error in the calculation can change the sign of the Tolman length. The curvature dependent surface tension of vapor bubbles in liquid is another way to test the value of the Tolman length. While the gREM simulation does adequately sample the spherical bubble state, we found it difficult to hold this state in a single replica long enough to get good statistics due to exchange. This should not affect the thermodynamic calculations since the bubble state gets sampled well over different replicas. The analysis of bubbles will be the focus of future work.

Finally, it has been noted that a translational entropy term needs to be added to Eq. (13) to account for the finite size effects of the simulation.[81] When we tried to fit gREM simulation data with the additional logarithmic term accounting for the translational entropy, we found that there was no significant difference in the fit or the Tolman length obtained.

Once the surface tension is known, the variation of the free energy with R for the precritical and postcritical nuclei can also be calculated. Instead of using the R-dependent surface tension, we just use the surface tension of the critical nuclei,

$$\Delta G(R) \approx \frac{4}{3}\pi R^3 \rho_l \Delta\mu + 4\pi R^2 \gamma(R^*). \tag{31}$$

We have made the assumption that the surface tension of the critical nuclei is a good approximation for the whole range of R. This should be a better approximation than CNT where the planar surface tension is used. Figure 10 shows the comparison of the whole free energy profile with that obtained by ten Wolde and Frenkel using umbrella sampling.[21] The nucleus size in the umbrella sampling used a classification scheme using the coordination number within a certain cutoff, while in gREM, the nucleus size N is calculated as $4/3\pi R_s^3 \rho_l$.

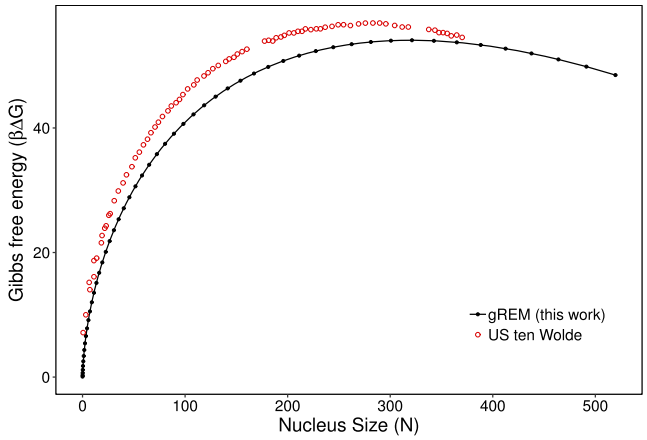

FIG. 10. Nucleation free energy varying with the nucleus size at $T = 0.741$ and $P = 0.1202$. The classification scheme used in the umbrella sampling simulations by ten Wolde *et al.*[21] is that a particle is liquid-like if it has more than 4 neighbors and belongs to the same cluster. The cutoff used to define the number of neighbors is 1.5. The nucleus size N in the gREM simulation is calculated as equal to $4/3\pi R^3 \rho_l$.

V. NUCLEATION RATE

Finally, we compare the nucleation rate obtained from gREM simulation against the nucleation rate obtained by directly counting the number of nuclei present above a certain threshold value. We compare against two sets of data: the first is from Horsch *et al.*[82] who simulated 10^6 particles using LJ potential with a cutoff of 2.5σ and the second is from Diemand *et al.*[23] who simulated 10^8 particles using a cutoff of 5σ. To compare against the latter dataset, we ran gREM with an LJ cutoff of 5σ. The nucleation rate is obtained using Eq. (14) where ΔG^* and $\Delta\mu$ are obtained from the gREM simulation as shown in Fig. 2. The number of particles in the critical cluster, N^*, is equal to $4/3\pi R_s^3 \rho_l$, and the surface area $A(N)$ is equal to $4\pi R_s^2$, where R_s is the surface of tension calculated using Eq. (7). The liquid density ρ_l used here is calculated from a parameterized form $\rho_l = 0.319 + 0.5649(T_c - T)^{1/3} + 0.1314(T_c - T) + 0.0413(T_c - T)^{3/2}$ for the cutoff $r_c = 2.5$ where the critical temperature is $T_c = 1.077\,9$ and $\rho_l = 0.023\,8 * (13.29 + 24.492 f^{0.35} + 8.155 f)$ for the larger cutoff of $r_c = 5\sigma$ where $f = (1 - T/1.257)$.[23,83] The vapor density is the same as the density of the entire box of the vapor branch in gREM at temperature T. We use the condensation coefficient value c obtained in the simulation by Diemand *et al.*[23] for the cutoff $r_c = 5\sigma$ and use an approximation for $r_c = 2.5\sigma$,[82,84]

$$c = \frac{b^2}{(b^2 + q^2)}, \tag{32}$$

where

$$q = \Delta h_v - 0.5 k_B T - \frac{2}{3}\frac{A(N)\gamma(R,T)}{N^*} \tag{33}$$

and

TABLE II. For LJ cutoff radius r_c = 2.5, comparison of the nucleation rate obtained from gREM (J_{gREM}) with direct simulation (J_{MD}) results[23] at different temperatures (T) and supersaturations ($S = P/P_{coex}$). ΔG^* and $\Delta\mu$ are the Gibbs free energy and chemical potential difference obtained from gREM. c is the condensation coefficient from Eq. (32) which has been used in Eq. (16).

T	S	P	$\beta\Delta G^*$	$\Delta\mu$	c	J_{MD}	J_{gREM}
0.8	1.791	0.02478	1.24	0.37	0.068	$2*10^{-9}$	$8.9 \pm 0.1*10^{-6}$
0.85	1.539	0.0329	0.80	0.26	0.084	$3*10^{-8}$	$3.2 \pm 0.3*10^{-5}$
0.9	1.31	0.04123	3.89	0.16	0.11	$6*10^{-9}$	$3.8 \pm 0.1*10^{-6}$

TABLE III. For LJ cutoff radius r_c = 5, comparison of the nucleation rate obtained from gREM (J_{gREM}) with direct simulation (J_{MD}) results[23] at temperature is T = 0.8 at different supersaturations ($S = PP_i/P_{coex}$). ΔG^* and $\Delta\mu$ are the Gibbs free energy and chemical potential difference obtained from gREM. c is the condensation coefficient from MD[23] which has been used in Eq. (16).

T	S	P	$\beta\Delta G^*$	$\Delta\mu$	c	J_{MD}	J_{gREM}
0.8	3.55	0.0161	8.58	0.87	0.11	$1.25 \pm 0.02*10^{-12}$	$2.8 \pm 0.1*10^{-9}$
0.8	3.33	0.0151	16.90	0.83	0.10	$3.38 \pm 0.26*10^{-14}$	$6.3 \pm 0.5*10^{-13}$

$$b^2 = (C_v + 0.5k_B)k_B T^2. \tag{34}$$

Δh_v is the bulk enthalpy of vaporization for which we use the parameterized form from Vrabec *et al.*[16] and C_v is the dimensionless isochoric heat capacity of the vapor which we approximate to the ideal gas value $3/2k_B$.

The comparison of nucleation rates obtained from gREM and from direct MD simulations, shown in Table II ($r_c = 2.5\sigma$) and Table III ($r_c = 5\sigma$), is reasonable. We note that gREM is most accurate for nuclei with larger cluster size whereas direct MD simulations are best for observing nucleation with small cluster sizes as these are the most accessible during MD. We reiterate that the calculation of the nucleation rate using gREM does not require any classification scheme to separate the vapor and liquid particles. The curvature is defined using the surface of tension R_s which is obtained from thermodynamic quantities [Eq. (7)].

VI. CONCLUSION

In this work, we have applied the generalized Replica Exchange Method (gREM) to study the vapor-liquid transition of Lennard-Jones spheres. gREM reproduces the coexistence values very well. The isobaric implementation of gREM leads to the planar interface having a bulk pressure higher than the set pressure. This makes the use of gREM for free energy and surface tension calculation of planar interfaces difficult in the case of vapor-liquid transition. The problem should not be this exaggerated for the solid-liquid transition since the pressure difference between the solid and liquid phases is not very large in that case and the gREM strategy is applicable even for the planar case in solid-liquid equilibrium. For the case of the spherical interface, the nucleation free energy obtained from gREM is in good comparison with the literature values. The curvature dependent surface tension was then obtained using the free energy and chemical potential values from gREM. This was, in turn, used to obtain the Tolman length which compares reasonably well with the literature values. Finally, the nucleation rate obtained from gREM is compared against the values from direct simulations.

This work shows the usefulness of the gREM technique for studying nucleation of spherical droplets. A major advantage of gREM over umbrella sampling and related methods is that multiple critical nuclei at different conditions can be simultaneously studied. This is because gREM obtains the free energy difference between the nuclei state and the bulk by integrating over a path of critical nuclei formed at different conditions. In contrast, umbrella sampling integrates along a path of nuclei at the same thermodynamic state but ones that are not mechanically stable (precritical) nuclei. Another advantage is that the free energy obtained in gREM is free of any classification scheme.

ACKNOWLEDGMENTS

This work was supported by the Division of Material Sciences and Engineering, Office of Basic Energy Sciences, U.S. Department of Energy, under Contract No. DE-AC02-07CH11358 with Iowa State University. We also thank David Stelter and Tom Keyes for sharing the python scripts for postprocessing the gREM data from LAMMPS.

REFERENCES

[1] P. R. ten Wolde and D. Frenkel, "Enhancement of protein crystal nucleation by critical density fluctuations," Science **277**(5334), 1975–1978 (1997).
[2] J. Kirkby, J. Curtius, J. Almeida, E. Dunne, J. Duplissy, S. Ehrhart, A. Franchin, S. Gagné, L. Ickes, A. Kürten *et al.*, "Role of sulphuric acid, ammonia and galactic cosmic rays in atmospheric aerosol nucleation," Nature **476**(7361), 429 (2011).

[3]S. K. Goel and E. J. Beckman, "Generation of microcellular polymeric foams using supercritical carbon dioxide. I: Effect of pressure and temperature on nucleation. Polym. Eng. Sci. **34**(14), 1137–1147 (1994).
[4]A. Fladerer and R. Strey, "Homogeneous nucleation and droplet growth in supersaturated argon vapor: The cryogenic nucleation pulse chamber," J. Chem. Phys. **124**(16), 164710 (2006).
[5]V. I. Kalikmanov, J. Wölk, and T. Kraska, "Argon nucleation: Bringing together theory, simulations, and experiment," J. Chem. Phys. **128**(12), 124506 (2008).
[6]K. Iland, J. Wedekind, J. Wölk, and R. Strey, "Homogeneous nucleation of nitrogen," J. Chem. Phys. **130**(11), 114508 (2009).
[7]M. P. Anisimov, E. G. Fominykh, S. V. Akimov, and P. K. Hopke, "Vapor–gas/liquid nucleation experiments: A review of the challenges," J. Aerosol Sci. **40**(9), 733–746 (2009).
[8]P. R. ten Wolde, M. J. Ruiz-Montero, and D. Frenkel, "Numerical calculation of the rate of homogeneous gas–liquid nucleation in a Lennard-Jones system," J. Chem. Phys. **110**(3), 1591–1599 (1999).
[9]M. Volmer and A. Weber, "Keimbildung in übersättigten gebilden," Z. Phys. Chem. **119U**(1), 277–301 (1926).
[10]R. Becker and W. Döring, "Kinetische behandlung der keimbildung in übersättigten dämpfen," Ann. Phys. **416**(8), 719–752 (1935).
[11]D. W. Oxtoby, "Homogeneous nucleation: Theory and experiment," J. Phys.: Condens. Matter **4**(38), 7627 (1992).
[12]K. J. Oh and X. C. Zeng, "Formation free energy of clusters in vapor-liquid nucleation: A Monte Carlo simulation study," J. Chem. Phys. **110**(9), 4471–4476 (1999).
[13]A. Laaksonen, V. Talanquer, and D. W. Oxtoby, "Nucleation: Measurements, theory, and atmospheric applications," Annu. Rev. Phys. Chem. **46**(1), 489–524 (1995).
[14]R. McGraw and A. Laaksonen, "Scaling properties of the critical nucleus in classical and molecular-based theories of vapor-liquid nucleation," Phys. Rev. Lett. **76**(15), 2754 (1996).
[15]J. Merikanto, E. Zapadinsky, A. Lauri, and H. Vehkamäki, "Origin of the failure of classical nucleation theory: Incorrect description of the smallest clusters," Phys. Rev. Lett. **98**(14), 145702 (2007).
[16]J. Vrabec, G. Kumar Kedia, G. Fuchs, and H. Hasse, "Comprehensive study of the vapour–liquid coexistence of the truncated and shifted Lennard–Jones fluid including planar and spherical interface properties," Mol. Phys. **104**(09), 1509–1527 (2006).
[17]J. Julin, I. Napari, J. Merikanto, and H. Vehkamäki, "A thermodynamically consistent determination of surface tension of small Lennard-Jones clusters from simulation and theory," J. Chem. Phys. **133**(4), 044704 (2010).
[18]B. J. Block, S. K. Das, M. Oettel, P. Virnau, and K. Binder, "Curvature dependence of surface free energy of liquid drops and bubbles: A simulation study," J. Chem. Phys. **133**(15), 154702 (2010).
[19]A. Tröster, M. Oettel, B. Block, P. Virnau, and K. Binder, "Numerical approaches to determine the interface tension of curved interfaces from free energy calculations," J. Chem. Phys. **136**(6), 064709 (2012).
[20]A. Malijevskỳ and G. Jackson, "A perspective on the interfacial properties of nanoscopic liquid drops," J. Phys.: Condens. Matter **24**(46), 464121 (2012).
[21]P. R. ten Wolde and D. Frenkel, "Computer simulation study of gas–liquid nucleation in a Lennard-Jones system," J. Chem. Phys. **109**(22), 9901–9918 (1998).
[22]M. Horsch, H. Hasse, A. K. Shchekin, A. Agarwal, S. Eckelsbach, J. Vrabec, E. A. Müller, and G. Jackson, "Excess equimolar radius of liquid drops," Phys. Rev. E **85**(3), 031605 (2012).
[23]J. Diemand, R. Angélil, K. K. Tanaka, and H. Tanaka, "Large scale molecular dynamics simulations of homogeneous nucleation," J. Chem. Phys. **139**(7), 074309 (2013).
[24]S. Auer and D. Frenkel, "Prediction of absolute crystal-nucleation rate in hard-sphere colloids," Nature **409**(6823), 1020 (2001).
[25]A. V. Brukhno, J. Anwar, R. Davidchack, and R. Handel, "Challenges in molecular simulation of homogeneous ice nucleation," J. Phys.: Condens. Matter **20**(49), 494243 (2008).
[26]B. Chen, J. I. Siepmann, K. J. Oh, and M. L. Klein, "Aggregation-volume-bias Monte Carlo simulations of vapor-liquid nucleation barriers for Lennard-Jonesium," J. Chem. Phys. **115**(23), 10903–10913 (2001).
[27]L. Filion, M. Hermes, R. Ni, and M. Dijkstra, "Crystal nucleation of hard spheres using molecular dynamics, umbrella sampling, and forward flux sampling: A comparison of simulation techniques," J. Chem. Phys. **133**(24), 244115 (2010).
[28]A. Haji-Akbari, R. S. DeFever, S. Sarupria, and P. G. Debenedetti, "Suppression of sub-surface freezing in free-standing thin films of a coarse-grained model of water," Phys. Chem. Chem. Phys. **16**(47), 25916–25927 (2014).
[29]F. Trudu, D. Donadio, and M. Parrinello, "Freezing of a Lennard-Jones fluid: From nucleation to spinodal regime," Phys. Rev. Lett. **97**(10), 105701 (2006).
[30]W. Lechner, C. Dellago, and P. G. Bolhuis, "Role of the prestructured surface cloud in crystal nucleation," Phys. Rev. Lett. **106**(8), 085701 (2011).
[31]P. R. Ten Wolde, M. J. Ruiz-Montero, and D. Frenkel, "Numerical evidence for bcc ordering at the surface of a critical fcc nucleus," Phys. Rev. Lett. **75**(14), 2714 (1995).
[32]P. R. ten Wolde, M. J. Ruiz-Montero, and D. Frenkel, "Numerical calculation of the rate of crystal nucleation in a Lennard-Jones system at moderate undercooling," J. Chem. Phys. **104**(24), 9932–9947 (1996).
[33]G. M. Torrie and J. P. Valleau, "Nonphysical sampling distributions in Monte Carlo free-energy estimation: Umbrella sampling," J. Comput. Phys. **23**(2), 187–199 (1977).
[34]U. H. E. Hansmann and Y. Okamoto, "Generalized-ensemble Monte Carlo method for systems with rough energy landscape," Phys. Rev. E **56**(2), 2228 (1997).
[35]Y. Okamoto, "Generalized-ensemble algorithms: Enhanced sampling techniques for Monte Carlo and molecular dynamics simulations," J. Mol. Graphics Modell. **22**(5), 425–439 (2004).
[36]B. A. Berg and T. Neuhaus, "Multicanonical algorithms for first order phase transitions," Phys. Lett. B **267**(2), 249–253 (1991).
[37]B. A. Berg and T. Neuhaus, "Multicanonical ensemble: A new approach to simulate first-order phase transitions," Phys. Rev. Lett. **68**(1), 9 (1992).
[38]A. P. Lyubartsev, A. A. Martsinovski, S. V. Shevkunov, and P. N. Vorontsov-Velyaminov, "New approach to Monte Carlo calculation of the free energy: Method of expanded ensembles," J. Chem. Phys. **96**(3), 1776–1783 (1992).
[39]E. Marinari and G. Parisi, "Simulated tempering: A new Monte Carlo scheme," EPL (Europhys. Lett.) **19**(6), 451 (1992).
[40]A. Mitsutake, Y. Sugita, and Y. Okamoto, "Generalized-ensemble algorithms for molecular simulations of biopolymers," Pept. Sci. **60**(2), 96–123 (2001).
[41]N. Hatano and J. E. Gubernatis, "A multicanonical Monte Carlo study of the 3D±J spin glass," Prog. Theor. Phys. Suppl. **138**, 442–447 (2000).
[42]U. H. E. Hansmann and Y. Okamoto, "The generalized-ensemble approach for protein folding simulations," in *Annual Reviews of Computational Physics VI* (World Scientific, 1999), pp. 129–157.
[43]J. Kim, T. Keyes, and J. E. Straub, "Replica exchange statistical temperature Monte Carlo," J. Chem. Phys. **130**(12), 124112 (2009).
[44]J. Kim, T. Keyes, and J. E. Straub, "Generalized replica exchange method," J. Chem. Phys. **132**(22), 224107 (2010).
[45]P. Virnau and M. Müller, "Calculation of free energy through successive umbrella sampling," J. Chem. Phys. **120**(23), 10925–10930 (2004).
[46]K. Binder, B. J. Block, P. Virnau, and A. Tröster, "Beyond the Van Der Waals loop: What can be learned from simulating Lennard-Jones fluids inside the region of phase coexistence," Am. J. Phys. **80**(12), 1099–1109 (2012).
[47]S. Plimpton, "Fast parallel algorithms for short-range molecular dynamics," J. Comput. Phys. **117**(1), 1–19 (1995).
[48]E. Małolepsza, M. Secor, and T. Keyes, "Isobaric molecular dynamics version of the generalized replica exchange method (gREM): Liquid–vapor equilibrium," J. Phys. Chem. B **119**(42), 13379–13384 (2015).
[49]Q. Lu, J. Kim, and J. E. Straub, "Order parameter free enhanced sampling of the vapor-liquid transition using the generalized replica exchange method," J. Chem. Phys. **138**(10), 104119 (2013).
[50]J. S. Rowlinson and B. Widom, *Molecular Theory of Capillarity* (Courier Corporation, 2013).
[51]R. C. Tolman, "The effect of droplet size on surface tension," J. Chem. Phys. **17**(3), 333–337 (1949).

[52]S. S. Rekhviashvili and E. V. Kishtikova, "On the size dependence of the surface tension," Tech. Phys. **56**(1), 143–146 (2011).
[53]E. M. Blokhuis and J. Kuipers, "Thermodynamic expressions for the Tolman length," J. Chem. Phys. **124**(7), 074701 (2006).
[54]A. E. van Giessen and E. M. Blokhuis, "Direct determination of the Tolman length from the bulk pressures of liquid drops via molecular dynamics simulations," J. Chem. Phys. **131**(16), 164705 (2009).
[55]A. E. van Giessen, E. M. Blokhuis, and D. Jan Bukman, "Mean field curvature corrections to the surface tension," J. Chem. Phys. **108**(3), 1148–1156 (1998).
[56]W. Helfrich, Z. Nat. C **28**, 693 (1973).
[57]A. M. Ferrenberg and R. H. Swendsen, "New Monte Carlo technique for studying phase transitions," Phys. Rev. Lett. **61**(23), 2635 (1988).
[58]A. M. Ferrenberg and R. H. Swendsen, "Optimized Monte Carlo data analysis," Comput. Phys. **3**(5), 101–104 (1989).
[59]S. Kumar, J. M. Rosenberg, D. Bouzida, R. H. Swendsen, and P. A. Kollman, "The weighted histogram analysis method for free-energy calculations on biomolecules. I. The method," J. Comput. Chem. **13**(8), 1011–1021 (1992).
[60]S. Xu, X. Zhou, and Z.-C. Ou-Yang, "Parallel tempering simulation on generalized canonical ensemble," Commun. Comput. Phys. **12**(5), 1293–1306 (NOV 2012).
[61]A. E. García and J. N. Onuchic, "Folding a protein in a computer: An atomic description of the folding/unfolding of protein A," Proc. Natl. Acad. Sci. U. S. A. **100**(24), 13898–13903 (2003).
[62]P. Poulain, F. Calvo, R. Antoine, M. Broyer, and P. Dugourd, "Performances of Wang-Landau algorithms for continuous systems," Phys. Rev. E **73**(5), 056704 (2006).
[63]H. Fukunishi, O. Watanabe, and S. Takada, "On the Hamiltonian replica exchange method for efficient sampling of biomolecular systems: Application to protein structure prediction," J. Chem. Phys. **116**(20), 9058–9067 (2002).
[64]J. Kim, T. Keyes, and J. E. Straub, "Communication: Iteration-free, weighted histogram analysis method in terms of intensive variables," J. Chem. Phys. **135**, 061103 (2011).
[65]L. G. Rizzi and N. A. Alves, "Communication: Multicanonical entropy-like solution of statistical temperature weighted histogram analysis method," J. Chem. Phys. **135**, 141101 (2011).
[66]M. S. Church, C. E. Ferry, and A. E van Giessen, "Thermodynamics of peptide dimer formation," J. Chem. Phys. **136**(24), 245102 (2012).
[67]D. Stelter, grem, https://github.com/dstelter92/gREM, 2017.
[68]T. Nakamura, S. Kawamoto, and W. Shinoda, "Precise calculation of the local pressure tensor in cartesian and spherical coordinates in LAMMPS," Comput. Phys. Commun. **190**, 120–128 (2015).
[69]J. H. Irving and J. G. Kirkwood, "The statistical mechanical theory of transport processes. IV. The equations of hydrodynamics," J. Chem. Phys. **18**(6), 817–829 (1950).
[70]S. J. Hub, L. B. De Groot, and D. van Der Spoel, "g_wham—A free weighted histogram analysis implementation including robust error and autocorrelation estimates," J. Chem. Theory Comput. **6**(12), 3713–3720 (2010).
[71]K. Binder, "Theory of the evaporation/condensation transition of equilibrium droplets in finite volumes," Physica A **319**, 99–114 (2003).
[72]M. Raju, D. Ballal, and X. Song, "Generalized ensemble studies of solid-liquid interface," unpublished results (2019).
[73]S. Prestipino, "The barrier to ice nucleation in monatomic water," J. Chem. Phys. **148**(12), 124505 (2018).
[74]P. M. Piaggi, O. Valsson, and M. Parrinello, "A variational approach to nucleation simulation," Faraday Discuss. **195**, 557–568 (2016).
[75]D. Li, J. Gaydos, and A. W. Neumann, "The phase rule for systems containing surfaces and lines. 1. moderate curvature," Langmuir **5**(5), 1133–1140 (1989).
[76]E. M. Blokhuis and A. E. van Giessen, "Density functional theory of a curved liquid–vapour interface: Evaluation of the rigidity constants," J. Phys.: Condens. Matter **25**(22), 225003 (2013).
[77]Y. A. Lei, T. Bykov, S. Yoo, and X. C. Zeng, "The Tolman length: Is it positive or negative?," J. Am. Chem. Soc. **127**(44), 15346–15347 (2005).
[78]A. E. van Giessen and E. M. Blokhuis, "Determination of curvature corrections to the surface tension of a liquid–vapor interface through molecular dynamics simulations," J. Chem. Phys. **116**(1), 302–310 (2002).
[79]Ø. Wilhelmsen, D. Bedeaux, and D. Reguera, "Tolman length and rigidity constants of the Lennard-Jones fluid," J. Chem. Phys. **142**(6), 064706 (2015).
[80]M. J. Haye and C. Bruin, "Molecular dynamics study of the curvature correction to the surface tension," J. Chem. Phys. **100**(1), 556–559 (1994).
[81]A. Tröster, F. Schmitz, P. Virnau, and K. Binder, "Equilibrium between a droplet and surrounding vapor: A discussion of finite size effects," J. Phys. Chem. B **122**(13), 3407–3417 (2017).
[82]M. Horsch, J. Vrabec, and H. Hasse, "Modification of the classical nucleation theory based on molecular simulation data for surface tension, critical nucleus size, and nucleation rate," Phys. Rev. E **78**(1), 011603 (2008).
[83]V. G. Baidakov, S. P. Protsenko, Z. R. Kozlova, and G. G. Chernykh, "Metastable extension of the liquid-vapor phase equilibrium curve and surface tension," J. Chem. Phys. **126**(21), 214505 (2007).
[84]J. Feder, K. C. Russell, J. Lothe, and G. M. Pound, "Homogeneous nucleation and growth of droplets in vapours," Adv. Phys. **15**(57), 111–178 (1966).